# Learning vortex induced vibrations from riser field experimental strain data.

Andreas P. Mentzelopoulos[a,b]

[a]Parallel Computing & Scientific Machine Learning (18.337), Spring 2023, Massachusetts Institute of Technology
[b]Department of Mechanical Engineering, Massachusetts Institute of Technology

ARTICLE INFO

*Keywords*:
Scientific Machine Learning
Unsupervised Learning
Nonconvex Optimization
Regression
Optimal Sparse Modal Expansion
Stochastic Mode Search

ABSTRACT

We show how to reconstruct the vortex-induced vibrations of a riser from experimental strain measurements using a machine learning framework. We employ a modal decomposition technique followed by inference of the expansion modes using a two-stage optimization routine. A stochastic mode search algorithm is developed and its capabilities and limitations are demonstrated using the MIAMI II riser field experiments, conducted in the Gulf Stream off the coast of Miami, FL using a densely instrumented riser model. Validation is done according to a k-fold cross-validation scheme. Computations are accelerated by paralellizing repeated tasks.

## 1. Introduction

Vortex induced vibrations (VIV) are driven by the periodic shedding of vortices formed in the wake behind bluff bodies placed within currents [1]. The vibration amplitude does not typically exceed one to two body diameters [2]. Rigid cylinder VIV have become the canonical problem for study of the phenomenon [3, 4, 5]. Flexible body VIV are similar to rigid body vibrations as they are driven by vortex sheeding, but with the added complexity that the loading is non-uniform along the span as the flexible body undergoes spatially traveling and/or standing waves.

Riser motion reconstruction has been done by leveraging the physics-based modal expansion technique [6, 7, 8] developed to model vibrations of continuous flexible bodies, such as beams [9]. In this work, the modal expansion approach is employed, followed by a data-informed selection of the expansion modes to restrict the model's complexity while satisfying the motion constraints imposed by VIV physics. The challenge is that a large number of parameters are involved in riser modeling, a problem which is common within the field of regression and has led to a variety of techniques for variable subset selection [10]. This framework is used to satisfy physics-based VIV motion constraints (for example, amplitude restriction), while still utilizing the modal decomposition model.

## 2. Methodology

### 2.1. Data Description

The MIAMI II experiments took place in October 2006 with purpose to conduct high mode number VIV experiments in the stream of the Gulf of Mexico. The tests were conducted using a composite pipe of Length $L = 152.524$ m and drag diameter $D = 0.0363$ m. A depiction of the experimental setup is included in Fig 8. Strain data were collected at 70 uniformly spaced locations (every $\Delta z = 2.1335$ m) excluding the endpoints of the body sampled at $f_{sampling} = 50.4857$ Hz. For more information on the experiments one should refer to [11, 12, 13, 14]. For this work, the cross-flow strain data collected from experiment 20061020164517 between time 50-70 seconds are used.

### 2.2. Modelling the flow induced motions

Consider a flexible riser of circular cross-section with radius $R$, spanning a length $L$. Let the amplitude response be approximated by a modal decomposition as follows.

$$y(z,t) = \sum_{n\in S} c_n(t)\,\phi_n(z) \tag{1}$$

where $c_n(t)$ are time varying coefficients and $\phi_n(z)$ are the corresponding mode shapes. For VIV in the cross-flow direction we expect sinusoidal mode shapes with time varying amplitudes [1]. A reasonable choice for the modes could thus be Fourier modes as in Equation 2.

$$y(z,t) = \alpha_0(t) + \sum_{n\in S}\left[\alpha_n(t)\,\cos(\frac{n\pi}{L}z) + \beta_n(t)\,\sin(\frac{n\pi}{L}z)\right] \tag{2}$$

where the contributing expansion modes are in set $S$ and the coefficients $\alpha_n$ and $\beta_n$ are varying in time, i.e. $\alpha_n = \alpha_n(t)$ and $\beta_n = \beta_n(t)$. Allowing the set $S \neq \mathbb{N}_+$ in Equation 2 yields a Fourier series with selectively omitted modes. For simplicity, one may rewrite Equation 2 as follows.

$$y(z,t) = \mathrm{Re}\left[\sum_{n\in\mathbb{S}} c_n(t)\exp(\frac{in\pi}{L}z)\right] \tag{3}$$

where $i$ is the imaginary unit and the real symmetric set $\mathbb{S} = \{-S \cup \{0\} \cup S\}$ replaces set $S$.

For a riser with a circular cross-section the strain measured on the riser's surface may be related to its curvature as follows [15].

$$\kappa(z,t) = \frac{\varepsilon_{CF}(z,t)}{R} \approx \frac{\partial^2 y(z,t)}{\partial z^2} \tag{4}$$

where $\varepsilon_{CF}$ is the CF strain, and $\kappa$ is the riser's curvature. Leveraging Equation 3 this is equivalent to

$$\frac{\partial^2 y(z,t)}{\partial z^2} = \mathrm{Re}\left[\sum_{n\in\mathbb{S}} -(\frac{n\pi}{L})^2 c_n(t)\exp(\frac{in\pi}{L}z)\right] = \frac{\varepsilon_{CF}(z,t)}{R} \tag{5}$$

Equation 5 may thus be used to formulate a system of linear equations to determine the coefficients $c_n(t)$ (at each time instance) assuming the set $\mathbb{S} \neq \mathbb{N}_+$ is known a priori and only limited measurements of the strain are available. The ordinary least squares problem formulation is as follows.

$$c_n(t_0) = \arg\min_{c_n}\left\{\sum_{z_i=0}^{z_i=L}\left\{\mathrm{Re}\left[\sum_{n\in\mathbb{S}} -(\frac{n\pi}{L})^2 c_n \exp(\frac{in\pi}{L}z_i)\right] - \frac{\varepsilon_{CF}(z_i,t_0)}{R}\right\}^2\right\} \tag{6}$$

where $n \in \mathbb{S} \neq \mathbb{N}_+$.

### 2.3. Machine learning vortex induced vibrations

Let the function $y(z,t)$ defined in Equation 2 be used as a trial function to approximate the VIV motions. It follows from Equation 4 that

$$\int_L \left|\frac{d^2 y(z,t_0)}{dz^2} - \frac{\varepsilon_{CF}(z,t_0)}{R}\right| dz = 0 \tag{7}$$

Equation 7 thus may be used to quantify the approximation quality of $y(z,t_0)$ in terms of approximating the true motions at time instance $t_0$ by measuring the deviation of the integral from zero. Extending the definition across all time instances (which are discrete) an objective function measuring approximation quality for $y(z,t)$ may be formulated as follows.

$$\mathbf{J}(y = f(z,t)) = \sum_t \int_L \left|\frac{\partial^2 y(z,t)}{\partial z^2} - \frac{\varepsilon_{CF}(z,t)}{R}\right| dz \tag{8}$$

We underscore that minimizing Equation 8 is a necessary but not sufficient condition to optimally approximate the riser's VIV motions, we further need to satisfy VIV physics-based constraints. Combining Equations 2 and 8 an objective that can be used to learn the expansion modes, i.e. the discrete set $\mathbb{S}$ may be formulated as follows.

$$\mathbf{J}(\mathbb{S}) = \sum_t \int_L \left|\mathrm{Re}\left[\sum_{n\in\mathbb{S}} -(\frac{n\pi}{L})^2 c_n(t)\exp(\frac{in\pi}{L}z)\right] - \frac{\varepsilon_{CF}(z,t)}{R}\right| dz \tag{9}$$

A final remark is that both the coefficients $c_n(t)$ and the set $\mathbb{S}$ are learned from the data; however we note that the optimality of the coefficients $c_n(t)$ can only be defined after a choice for the set $\mathbb{S}$ is made. In addition, the coefficients $c_n(t)$ are not learned according to Equation 9 but are determined at each time instance by solving an OLS problem (Equation 6).

### 2.4. Constraints

We first consider the physical constraints imposed on a riser. For a pinned-free riser we expect

$$y(z=0,t) = 0 \;\; \forall t \in [0,T] \tag{10}$$

We note this is an essential boundary condition and should thus be hardly imposed. In addition, natural boundary conditions suggest that the bending moments at the body ends should be zero. The third derivative of the displacement at the free end should also be zero [8]. Thus,

$$\left.\frac{\partial^2 y(z,t)}{\partial z^2}\right|_{z=0} = \left.\frac{\partial^2 y(z,t)}{\partial z^2}\right|_{z=L} = \left.\frac{\partial^3 y(z,t)}{\partial z^3}\right|_{z=L} = 0 \;\; \forall t \in [0,T] \tag{11}$$

The natural boundary conditions are imposed softly. Finally, the amplitude constraint is as follows

$$\max_{z\in[0,L],\; t\in[0,T]} \{y(z,t), -y(z,t)\} < 2D \tag{12}$$

where $D$ is the cylinder's diameter. The amplitude constraint was strictly imposed. Lastly, given that the expected physical vibration mode is not to exceed 30, the expansion modes in $S$ are narrowed down to $S \subseteq \Omega$, where $\Omega = \{1,2,3,...,90\}$.

## 3. Results and Discussion

In this section we present the optimization algorithm reconstructions and attempt to validate the models obtained after applying the proposed methodologies on the experimental data. We note that all coding for this project was done in Julia and then the results were plotted using MATLAB. Both the Julia and the MATLAB codes are included in Appendix C. Indicative Julia plots of the results are included in Appendix B.

### 3.1. Optimization Routine

Optimizing the objective function in order to obtain the optimal set $\mathbb{S}$ is highly nontrivial. Essentially, the choice

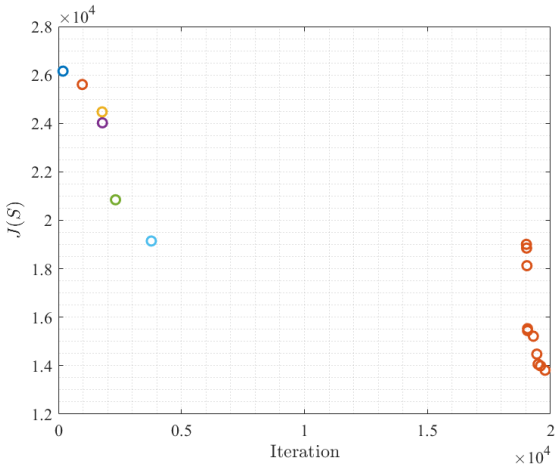


Figure 1: Objective function plotted against iteration.

of $\mathbb{S}$ fundamentally alters the nature of $y(z,t)$ as defined in Equation 3 by governing the number of terms used. Thus, calculating a gradient with respect to the unknown parameters is not possible. To make maters worse, the number of subsets of $\Omega$ are $2^{|\Omega|} = 2^{90}$ which is inexhaustibly large.

A two stage stochastic search approach was employed to minimize the objective. In the first stage, the cardinality of $\mathbb{S}$ was restricted (to some different value at each iteration) and the set $\mathbb{S}$ was drawn uniformly at random from $\Omega$. This stage was the "space exploration" stage. Mathematically,

$$\begin{aligned} N_1 \leq |\mathbb{S}| \leq N_2, \quad N_1, N_2 \in \Omega \\ \mathbb{S} \leftarrow \{s_i \Big| \left(s_i = rand \in \Omega\right) \wedge \left(s_i \neq s_j \; \forall \; i \neq j\right)\} \end{aligned} \tag{13}$$

where the notation *rand* means a number chosen uniformly at random (i.e. $rand \sim U(\{N_1, N_1+1, ..., N_2-1, N_2\})$. Given the choice of $\mathbb{S}$, the optimal coefficients $c_n$ (OLS sense) were determined at each time and the objective function was evaluated. The set which yielded the lowest value of the objective was then selected as the optimal in stage 1. We call this set $\mathbb{S}_1$.

The second stage served as a "refinement" stage, in which the set $\mathbb{S}_1$ was perturbed and the objective was evaluated. Perturbations included the following: (i) a few modes were added or removed from $\mathbb{S}$, (ii) some or all of the modes in $\mathbb{S}$ were altered slightly. Mathematically, both procedures fall into the below operations or their combination.

$$\begin{aligned} \mathbb{S} \leftarrow \mathbb{S}_1 \cup \mathbb{S}_p, \;\; \mathbb{S}_p = \\ \{s_i \Big| s_i \in \Omega \backslash \mathbb{S}_1 \wedge |s_i - x| < a \; for \; some \; x \in \mathbb{S}_1, a > 0\} \\ \mathbb{S} \leftarrow \mathbb{S}_1 \cup \mathbb{S}_p, \;\; \mathbb{S}_p = \{s_i \Big| s_i \in \Omega \; \wedge s_i \notin \mathbb{S}_1\} \\ \mathbb{S} \leftarrow \mathbb{S}_1 \backslash \mathbb{S}_p, \;\; \mathbb{S}_p \subset \mathbb{S}_1 \end{aligned} \tag{14}$$

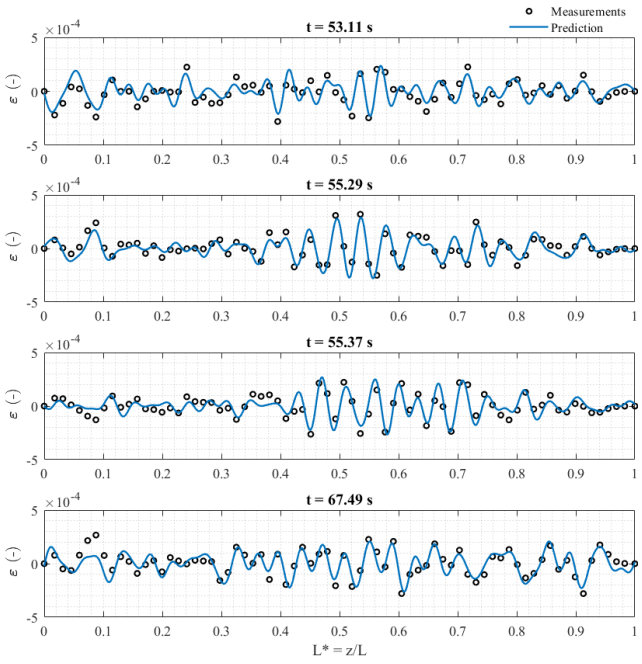


Figure 2: Strain measurements plotted on top of strain predictions as a function of body span for four randomly selected time instances. The model predictions after optimizing the modes are able to approximate the strain measurements closely. We underscore that the model not only agrees with measurements to reasonable accuracy but also satisfies the physics-based constraints which are applied on its second anti-derivative (not shown in this Figure).

The final set which yielded the lowest value of the objective function was then selected as the optimum. A pseudocode for the optimization routine is included in Appendix A.

### 3.2. Convergence and computational cost

Albeit the stochastic optimization algorithm lacks theoretical convergence guarantees, in practice convergence is observed. Specifically, after performing the algorithm with 10 restarts and performing 20,000 iterations with the last 1,000 iterations as the refinement stage, the returned set is the exact same all 10 times. In addition, if instead of 20,000 iterations only 5,000 iterations are performed, the optimal set obtained is the same as that obtained using 20,000 iterations for 7/10 restarts. The 3 suboptimal sets differed from the optimal by no more than 4 modes (out of 36 modes selected total).

A typical plot of the objective function plotted against iteration is shown in Figure 1. We note that since the objective is not monotonically decreasing with iteration number, the value of the objective was only plotted if it was better than the previous best estimate. The first 19,000 iterations served as the exploration stage; we observe that the best set found in the exploration stage was found typically in less than 5,000 iterations. Rapid improvement to the final optimum was observed in the refinement stage (last 1,000 iterations).

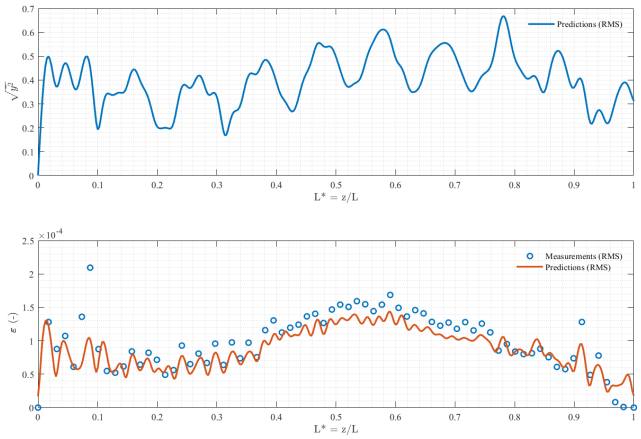


Figure 3: Time-wise root mean square (RMS) of measurements as well as of predictions of motion (top) and strain (bottom) as functions of body span.

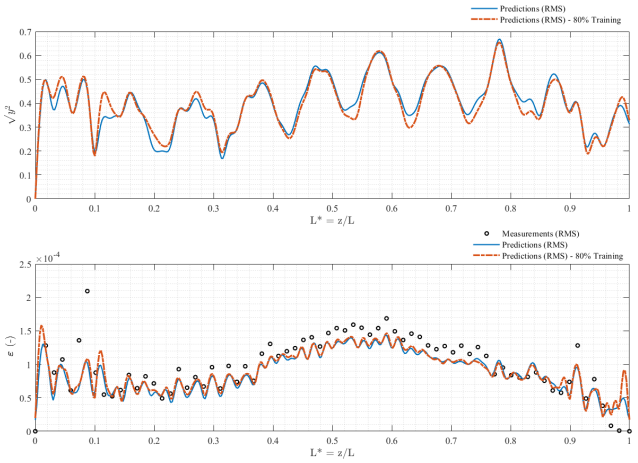


Figure 4: RMS motion (top) and RMS strain (bottom) as functions of span. Reconstructions are shown of a model trained on all available data (orange) and of a model trained on 80% of available data (blue) which predicts unseen data.

The wall time of the optimization is about one hour for 20,000 iterations on a computer with an intel core i7 CPU of 7th generation (2018). The process may be sped up by parallelizing loop operations, for example when computing the values of $y(z,t)$ which require extensive sequential summations and are repeated in the order of thousands of times at every iteration.

### 3.3. Validation

In order to examine how well the model approximates the motions after optimizing the expansion modes according to the nonlinear objective, model predictions were compared to observations at different times. Figure 2 illustrates the recorded strain measurements as well as the trained model predictions at four randomly sampled times. As is evident in the Figure, the model is able to approximate the motions to reasonable accuracy in all four times shown. In addition, the predictions follow the trends of the measurements as well as the fluctuations closely. We underscore that the model not only agrees with observations closely but also satisfies all constraints imposed.

Figure 3 illustrates the the time-wise root mean square (RMS) of measurements as well as of predictions of motion (top) and strain (bottom) as functions of body span. The RMS measurements and predictions are useful in illustrating the effectiveness of the model in terms of predictions throughout all recorded time steps.

As is evident in Figure 3 the RMS strain predictions show reasonable agreement with measurements. However, they do underpredict the strain slightly at about midspan. The RMS motions of the riser are reasonable resembling closely the vibrations of a flexible body oscillating in the tenth mode [9]. In addition, since the vibration of each location is sinusoidal, one can easily verify that the amplitude (on average) did not exceed $rms\{y(z,t)\} \times \sqrt{(2)}$ which remains below 1 diameter. We underscore that although on average the amplitude was about 1 diameter, time instances were recorded where the maximum amplitude remained barely below 2 diameters.

### 3.4. Generalization

In order to assess how well the optimized model generalizes, a five-fold cross validation was performed. Specifically, 16 seconds of the total 20 seconds of available data were used to train the model and testing was done on the unseen four seconds. We include cross validation plots for training using the first 16 seconds and testing on the full 20 seconds. Figure 4 illustrates the predicted RMS motion (top) as well as the reconstructed RMS strain (bottom). Besides experimental strain measurements, two reconstructions are shown both for the strain measurements and for the amplitudes (partially trained model and fully trained model).

As is evident in the figure, not only are both models reasonably accurate, they are in addition remarkably consistent. The cross-validation performed suggests that the model can generalize reasonably well.

## 4. Parallelization of computations

The wall time of the program to determine an optimal mode set is about one hour for 20,000 iterations on a computer with an intel core i7 CPU of 7th generation (2018). Most of the computation time is spent in solving for the optimal coefficients $c_n(t)$ for each recorded time (given the trial mode set) and in performing the sequential summations required to approximate $y(z,t)$ and $\frac{\partial^2 y(z,t)}{\partial z^2}$ at each time step with modal expansion sums. Both operations must be repeated over 1,000 times for every iteration of the algorithm and thus effort was placed to speed up those operations by parallelizing loop computations using Julia's built in Threads.@threads macro.

Specifically, in order to approximate the coefficients at each time step a system of over-determined matrix equations

$Ax = b$ must be solved where the number of equations is of $O(100)$ and the number of unknowns is of $O(70)$. Formulation of this system, including both the matrix $A$ and the vector $b$, was done in parallel using 4 CPU cores instead of 1. Julia's backslash solver which is also multi-threaded was used to return the system's solution.

In addition, the computation of the modal sums of $y(z,t)$ and $\frac{\partial^2 y(z,t)}{\partial z^2}$ required extensive sequential summations which were also performed in parallel. Specifically, the summations were done atomically, ensuring thread-safe operations on the shared variables between the 4 CPU cores using Julia's Threads.Atomic operations guidelines.

| Process | Speed up |
|---|---|
| Formation of $A$ | x1.7 |
| Formation of $b$ | x3 |
| Calculation of $y(z,t)$, $\frac{\partial^2 y(z,t)}{\partial z^2}$ | x2 |

Table 1: Parallelization

Table 1 summarizes the speed improvements for the three operations described above: formulation of $A$ matrix, formulation of $b$ vector, sequential summations. All processes were sped up by more than 150% while formulation of the b matrix was sped up by 300%.

## 5. Conclusions

In this work, the VIV motions of a riser were machine-learned from experimental strain data via solving a physics-based combinatorial optimization problem. The modal decomposition technique was employed and followed by inference of a carefully selected set of optimal expansion modes learned from experimental data.

Solving the learning problem requires optimizing a non-convex, nonlinear objective function with a variable number of unknown parameters subject to various constraints both essential and natural. In order to optimize the objective, the authors propose a stochastic mode search algorithm and demonstrate its capabilities and limitations. The optimization routine's convergence and computational cost are examined. Finally, the combined modelling and optimization routine framework is studied and validated using a k-fold cross-validation scheme.

## A. Algorithms

**Algorithm 1** Stochastic Mode Search ($J(\mathbb{S})$)

$\mathbb{S}_{best} \leftarrow random\ set$
$J_{best} \leftarrow +\infty$
**for** i = number of total iterations **do**
  **if** i in explration stage **then**
    $\mathbb{S} \leftarrow random\ set \subseteq \Omega$
  **else if** i in refinement stage **then**
    $\mathbb{S} \leftarrow perturbation\ of\ \mathbb{S}_{best}$
  **end if**

  **for** t = recorded times **do**
    $c_n(t) \leftarrow \arg\min_{c_n} (Y''(z) - \frac{\varepsilon_{CF}(z,t)}{R})^2$
  **end for**

  **if** $J(\mathbb{S}) < J_{best}$ **then**
    $J_{best} \leftarrow J(\mathbb{S})$
    $\mathbb{S}_{best} \leftarrow \mathbb{S}$
  **end if**
**end for**
**return** $\mathbb{S}_{best}$

## B. Julia Figures

Using MATLAB as the plotting software of choice was mainly motivated by the fact that subplots with multiple data plotted in each subplot was not easy to do in Julia (I am new to Julia). These can in addition be used for comparison between plotting capabilities with Julia and MATLAB.

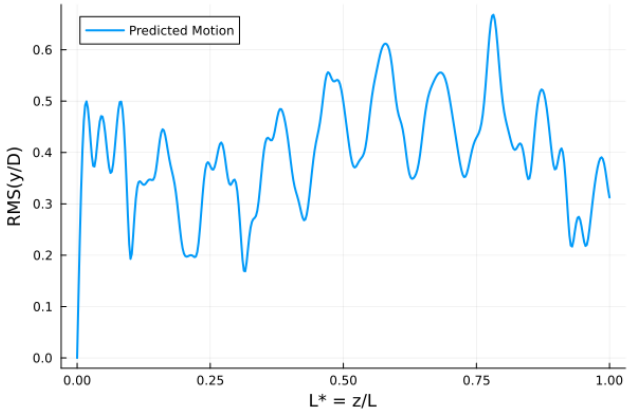


Figure 5: Time-wise root mean square (RMS) of measurements as well as of predictions of motion (top) and strain (bottom) as functions of body span plotted in Julia.

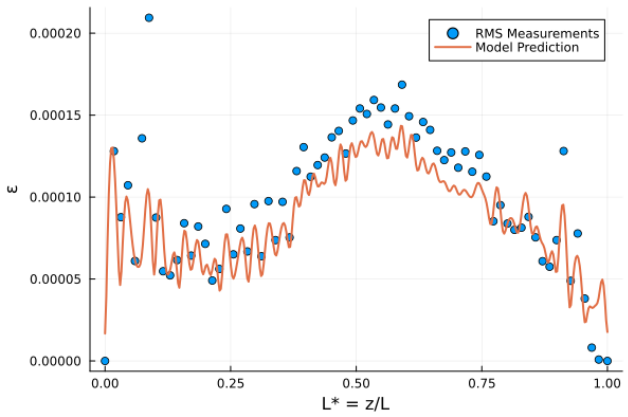


Figure 6: Time-wise root mean square (RMS) of measurements as well as of predictions of motion (top) and strain (bottom) as functions of body span plotted in Julia.

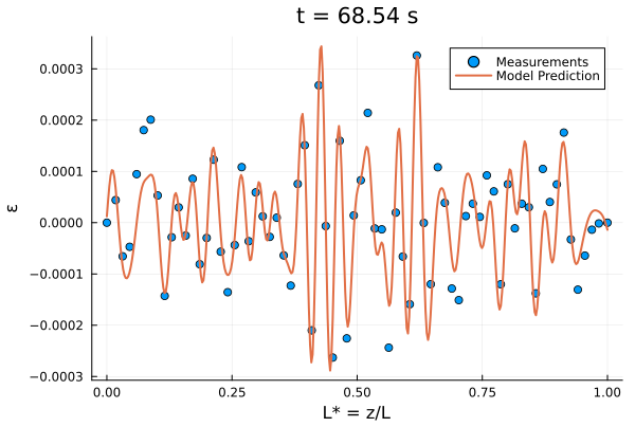


Figure 7: Strain measurements plotted on top of strain predictions as a function of body for a randomly selected time instance. The model predictions after optimizing the modes are able to approximate the strain measurements closely. We underscore that the model not only agrees with measurements to reasonable accuracy but also satisfies the physics-based constraints which are applied on its second anti-derivative (not shown in this Figure).

## C. Code

A public github repository has been created containing the relevant codes to the project (Both Julia and MATLAB codes). The link to the repository is:

https://github.com/mentzelopoulos/SciML-Project-18.337-Spring-2023-MIT.git

The required input data are also available in the github repository. Table 2 details the project files.

Recommendations for running the code: set "minmode" to be greater than 17. In addition run at least a few thousand iterations. Store the solutions by running the very last part of the code and they should be ready to be read by the MATLAB code.

| Filename | Purpose |
|---|---|
| sci_ml_project_v2.jl | Main Code (Julia) |
| Plotting_project.m | Plotting code (MATLAB) |
| fs.csv | Input file |
| t.csv | Input file |
| vel.csv | Input file |
| xCF.csv | Input file |
| z.csv | Input file |

Table 2: Relevant Codes on Github Repository

## D. Supplementary Figures

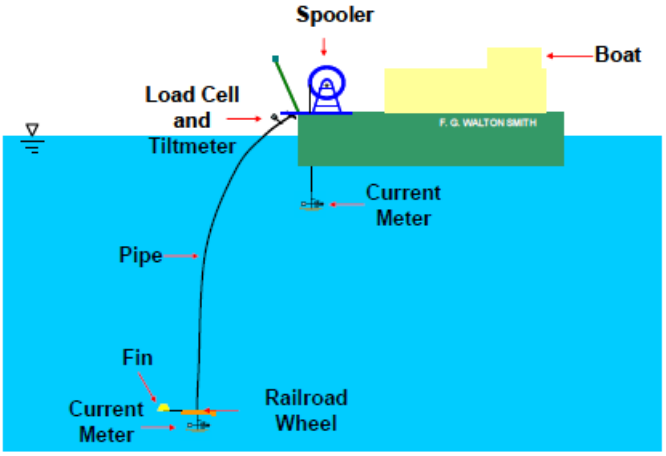


Figure 8: Depiction of experimental setup

## References

[1] Michael S Triantafyllou, Rémi Bourguet, Jason Dahl, and Yahya Modarres-Sadeghi. Vortex-induced vibrations. In *Springer Handbook of Ocean Engineering*, pages 819–850. Springer, 2016.

[2] Michael M Bernitsas, James Ofuegbe, Jau-Uei Chen, and Hai Sun. Eigen-solution for flow induced oscillations (viv and galloping) revealed at the fluid-structure interface. In *ASME 2019 38th International Conference on Ocean, Offshore and Arctic Engineering*. American Society of Mechanical Engineers Digital Collection, 2019.

[3] C.H.K. Williamson and A. Roshko. Vortex formation in the wake of an oscillating cylinder. *Journal of Fluids and Structures*, 2(4):355–381, 1988.

[4] MM Zdravkovich. Different modes of vortex shedding: an overview. *Journal of fluids and Structures*, 10(5):427–437, 1996.

[5] Wei Wu, Michael M Bernitsas, and Kevin Maki. Rans simulation versus experiments of flow induced motion of circular cylinder with passive turbulence control at 35,000 << 130,000. *Journal of Offshore Mechanics and Arctic Engineering*, 136(4), 2014.

[6] Harish Mukundan. *Vortex-induced vibration of marine risers: motion and force reconstruction from field and experimental data*. PhD thesis, Massachusetts Institute of Technology, 2008.

[7] Jungao Wang, Shixiao Fu, Rolf Baarholm, Mengmeng Zhang, and Chang Liu. Global motion reconstruction of a steel catenary riser under vessel motion. *Ships and Offshore Structures*, 14(5):442–456, 2019.

[8] M. S. Triantafyllou, G. S. Triantafyllou, Y. S. Tein, and B. D. Ambrose. Pragmatic riser viv analysis. In *Offshore Tech. Conf.* Offshore Technology Conference, 1999.

[9] S Rao Singiresu et al. *Mechanical vibrations*. Addison Wesley Boston, MA, 1995.

[10] Isabelle Guyon and André Elisseeff. An introduction to variable and feature selection. *J. Mach. Learn. Res.*, 3(null):1157–1182, mar 2003.

[11] Vivek Jaiswal and J Kim Vandiver. Viv response prediction for long risers with variable damping. In *International Conference on Offshore Mechanics and Arctic Engineering*, volume 4269, pages 901–909, 2007.

[12] Vikas Jhingran and J Kim Vandiver. Incorporating the higher harmonics in viv fatigue predictions. In *International Conference on Offshore Mechanics and Arctic Engineering*, volume 4269, pages 891–899, 2007.

[13] Hayden Marcollo, Hemant Chaurasia, and J Kim Vandiver. Phenomena observed in viv bare riser field tests. In *International Conference on Offshore Mechanics and Arctic Engineering*, volume 4269, pages 989–995, 2007.

[14] Susan B Swithenbank and J Kim Vandiver. Identifying the power-in region for vortex-induced vibrations of long flexible cylinders. In *International Conference on Offshore Mechanics and Arctic Engineering*, volume 4269, pages 723–730, 2007.

[15] H Mukundan, FS Hover, and MS Triantafyllou. A systematic approach to riser viv response reconstruction. *Journal of fluids and structures*, 26(5):722–746, 2010.